coatings

MDPI

Article

Carbon Dots Enable Low-Voltage Memristor Based on $CsPbBr_3$ for Artificial Synapses

Yilin Fan [1], Caiyi Shang [2], Leijun Zhou [1], Kuncheng Wang [1], Huiyun Zhang [3], Qingyu Xu [2,*] and Guangyu Wang [1,*]

[1] School of Physics Science & Information Technology, Liaocheng University, Liaocheng 252059, China
[2] School of Physics, Southeast University, Nanjing 210023, China
[3] School of Mechanical Engineering, North University of China, Taiyuan 030031, China
* Correspondence: xuqingyu@seu.edu.cn (Q.X.); wangguangyu@lcu.edu.cn (G.W.)

Highlights

What are the main findings?

- We developed a CDs-modified CsPbBr3 memristor achieving low switching voltage (<0.75 V) and enhanced cycling stability.
- We demonstrated synaptic plasticity emulation including long-term potentiation (LTP) and long-term depression (LTD) under electrical stimulation.
- Our study enabled wavelength-tunable resistive switching at 520 nm via optoelectronic co-stimulation, mimicking biological visual adaptability.

Abstract

Optoelectronic memristors show significant potential for neuromorphic computing but are often limited by high operating voltages. Here, we constructed a low-voltage $Ag/CsPbBr_3/CDs/FTO$ photonic memristor by incorporating carbon dots (CDs) as a regulatory medium within the $CsPbBr_3$ perovskite layer. The CDs significantly enhanced memristive performance: their surface defect states and localized electric field regulation enabled stable conductive filament formation and rupture at low voltages. This yielded favorable operational characteristics, including low set/reset voltages (0.72 V/−0.60 V) and preliminary cycling endurance with state retention. Leveraging the device's continuously tunable conductance, we successfully emulated key synaptic learning behaviors such as paired-pulse facilitation (PPF) and long-term potentiation/depression (LTP/LTD). Implementing its weight-updating characteristics in an artificial neural network (ANN) achieved 92.17% accuracy in handwritten digit classification. This work demonstrates the effective role of CDs in enabling low-voltage, high-performance perovskite photonic memristors, providing a viable strategy for developing low-power neuromorphic hardware.

Keywords: carbon dot; memristor; artificial synapses; conductive filaments

Check for updates

Academic Editor: Alessandro Latini

Received: 28 September 2026
Revised: 12 October 2026
Accepted: 12 October 2026
Published: 15 October 2026

Copyright: © 2026 by the authors. Licensee MDPI, Basel, Switzerland. This article is an open access article distributed under the terms and conditions of the Creative Commons Attribution (CC BY) license.

1. Introduction

The rapid advancement of artificial intelligence (AI) necessitates enhanced energy efficiency and parallel processing capabilities in computing systems to handle massive data in real time. The conventional von Neumann architecture, characterized by the physical separation of memory and processing units, incurs significant time delays and high energy consumption due to frequent data transfer between these components [1].

Neuromorphic computing, inspired by biological neural systems, overcomes this limitation by emulating neuronal and synaptic information processing at the hardware level [2]. This approach enables highly parallel, low-power in-memory computing, positioning it as a crucial solution to the bottlenecks inherent in traditional computing architectures [3].

Artificial synaptic devices constitute the core of neuromorphic hardware. Memristors are widely employed to emulate synaptic plasticity owing to their advantageous properties, including a simple structure, scalability, low power consumption, fast switching speed, and continuously tunable conductance [4]. In a typical metal/functional layer/conductive substrate structure, the top and bottom electrodes correspond to the presynaptic and postsynaptic membranes, respectively, while the intermediate functional layer represents the synaptic cleft [5]. Applying external stimuli, such as voltage, light, or a combination thereof, modulates carrier transport and defect state distribution within the device, thereby altering its conductance to simulate synaptic weight [6].

Various material systems, including metal oxides, perovskites, quantum dots, and transition metal dichalcogenides (TMDs), are employed in constructing optoelectronic synaptic devices. Halide perovskites are considered promising candidates due to their tunable bandgap, low exciton binding energy, high optical absorption coefficient, excellent carrier diffusion length, and inherent non-volatile memory effects. However, existing systems exhibit significant limitations. Traditional metal oxides (e.g., Ga_2O_3) primarily respond within the ultraviolet spectrum and exhibit weak visible-light optoelectronic regulation [7,8]. Two-dimensional layered materials (e.g., MoS_2, WS_2) suffer from weak photoresponse signals, high fabrication costs, and poor scalability [9–13]. Chalcogenides (e.g., GeTe, Sb_2S_3) demonstrate poor stability and limited optoelectronic response speeds [14–16]. Organic and hybrid perovskites (e.g., $FA_{0.83}Cs_{0.17}Pb(I_{0.7}Br_{0.3})_3$, $FA_{0.83}Cs_{0.17}PbI_3$) face challenges including degradation of organic components, poor thermal/moisture/oxygen stability, and a short cycle life, hindering their ability to meet simultaneous requirements for high-performance modulation and long-term stability [17,18]. In contrast, all-inorganic halide perovskites, with superior optoelectronic coupling and controllable memristive behavior, represent an emerging material class with significant potential for overcoming these limitations.

Among inorganic perovskites, $CsPbBr_3$ stands out owing to its low exciton binding energy, excellent carrier mobility, and efficient green-light absorption [19]. As memristive functional layer, it enables devices with low power consumption, tunable memristive characteristics, favorable optoelectronic response, and cost-effective fabrication [20], positioning it as an ideal candidate for high-performance optoelectronic synapses and neuromorphic vision hardware. Meanwhile, carbon dots (CDs), characterized by their small size, abundant surface functional groups, strong light absorption, and low cost, can introduce multi-tiered trap energy levels via surface defects and polar functional groups [21]. These characteristics facilitate the reversible trapping and controlled release of photogenerated carriers, providing an effective strategy to optimize memristor conductance modulation and enhance synaptic biomimetic performance.

In the present study, we fabricated three heterostructure devices: Ag/$CsPbBr_3$/FTO, Ag/CDs/$CsPbBr_3$/FTO, and Ag/$CsPbBr_3$/CDs/FTO. Within these devices, $CsPbBr_3$ functions as the primary memristive layer, while CDs serve as a carrier-modulating layer. This integrated design aims to enhance device performance by reducing operating voltages, improving cycling stability, and enabling optically tunable memristive behavior. Systematic characterization of $CsPbBr_3$'s crystal structure and optical properties using X-ray diffraction (XRD), scanning electron microscopy (SEM), X-ray photoelectron spectroscopy (XPS), and ultraviolet–visible (UV-vis; self-assembly) absorption spectroscopy confirmed its stable crystalline phase and significant light absorption. Memristive performance testing demon-

strated that the $CsPbBr_3$/CDs composite device exhibits lower switching voltages and superior cycling stability. Furthermore, under 520 nm illumination, this device achieved optically modulated memristive behavior and successfully emulated synaptic plasticity, including long-term potentiation (LTP) and long-term depression (LTD), under electrical stimulation. The optoelectronic synergy also enabled efficient neuromorphic information processing. Consequently, this study presents a novel strategy for developing low-power, high-stability optoelectronic synaptic devices and offers an alternative pathway for constructing neuromorphic hardware capable of mimicking biological visual perception.

2. Experimental Section

Synthesis of CDs: Hydrophobic CDs were synthesized via combustion. A mixture of octadecylamine, citric acid, and glycerol (1:1:7 molar ratio) was stirred continuously at 100 °C to form a homogeneous deep eutectic solvent precursor. This precursor was heated at 150 °C with continuous stirring until forming a black solid. The solid was ground and annealed at 350 °C under vacuum for 3 h to yield CDs. The product was dispersed in anhydrous ethanol via ultrasonication, forming CD dispersion. Thin films were fabricated through layer-by-layer drop-casting onto 80 °C FTO-coated glass substrates over 30 deposition cycles.

Device Fabrication: $CsPbBr_3$ thin films were fabricated via solution processing. $PbBr_2$ powder (1.101 g) was dissolved in Dimethylformamide (DMF) (3 mL) at 75 °C under stirring until complete dissolution, producing 1 mol/L solution. This solution was spin-coated (2000 rpm, 30 s) onto CD-film-coated FTO substrates preheated to 75 °C, then dried at 90 °C for 1 h to form $PbBr_2$ layers. CsBr powder (0.223 g) was dissolved in methanol (15 mL) to prepare 0.07 mol/L solution. The $PbBr_2$-coated films were immersed in this solution at 55 °C for 20 min for ion exchange, forming initial $CsPbBr_3$ films. After reaction, films were spin-washed with isopropanol (2000 rpm, 30 s) to remove residues. Following air-drying, annealing at 250 °C for 5 min optimized crystallinity, yielding dense, well-crystallized $CsPbBr_3$ films. Finally, Ag top electrodes were deposited via DC magnetron sputtering through shadow masks, completing device fabrication.

Device Characterization: Field-emission SEM (Hitachi Regulus 8100, Hitachi High-Tech Corporation, Tokyo, Japan) was employed to characterize the surface morphology of the $CsPbBr_3$ and CDs films, as well as to capture the cross-sectional image of the complete device for thickness measurement. XRD (Rigku Smartlab 9 kw, Cu Kα radiation, Rigaku Corporation, Tokyo, Japan) and XPS (Thermo Fisher Escalab 250xi, Al Kα radiation, Thermo Fisher Scientific, East Grinstead, UK) was utilized to analyze the crystal structure and phase purity of the $CsPbBr_3$ film, while X-ray photoelectron spectroscopy was used to determine the chemical composition and elemental valence states of the fabricated layers. The resistive switching behaviors of the memristor devices were characterized using a Keithley 2450 source meter (Tektronix (Keithley Instruments), Solon, OH, USA), which enabled precise control of applied voltages and measurement of corresponding current responses.

3. Results and Discussion

Optoelectronic memristors exhibit a structural and functional analogy to biological synapses. As depicted in Figure 1a, the top Ag electrode and bottom fluorine-doped tin oxide (FTO) electrode correspond to the presynaptic and postsynaptic membranes, respectively, while the intermediate photosensitive $CsPbBr_3$ memristive layer represents the synaptic cleft. Surface morphology analysis (Figure 1b) indicates that the $CsPbBr_3$ film comprises nanoscale grains and exhibits a dense structure. A cross-sectional SEM image of the Ag/$CsPbBr_3$/CDs/FTO device (Figure 1c) reveals a distinct interface between

the $CsPbBr_3$ film and FTO substrate, with a film thickness of approximately 374 nm. The XRD pattern (Figure 1d) displays diffraction peaks at 21.50°, 26.34°, 30.38°, 30.70°, and 37.60°, indexed to the (110), (111), (002), (200), and (211) planes of $CsPbBr_3$ [22]. These peak positions align well with the standard reference (PDF#18-0364) [23], confirming a well-crystallized film. The peak at 18.6° originates from the underlying carbon dot seed layer [24]. XPS analysis (Figure 1e) confirms the presence of Cs, Pb, and Br elements in the $CsPbBr_3$ film; an adsorbed carbon peak further indicates high purity. Following C 1s calibration (284.5 eV), the Cs 3d spectrum (Figure S1a) shows peaks at 723.6 eV ($3d_{5/2}$) and 737.5 eV ($3d_{3/2}$). The high-resolution Pb 4f spectrum (Figure S1b) exhibits a doublet at 137.6 eV ($4f_{7/2}$) and 142.5 eV ($4f_{5/2}$), while Br 3d states appear at 72.0 eV and 73.1 eV (Figure S1c), collectively confirming the expected chemical states [25]. The $CsPbBr_3$ absorption spectrum (Figure 1f) shows a steep edge at 516 nm, consistent with its visible light absorption [26]. The Tauc plot (Figure 1f inset) yields an optical bandgap of 2.34 eV. Additionally, the CD UV-Vis spectrum (Figure S2) shows an absorption peak at 290 nm attributed to π-π* transitions and surface states, indicating strong UV absorption [27]. Photoluminescence (PL) spectroscopy (Figure S3) reveals $CsPbBr_3$ emission peak at 524 nm and CD peak centered at 514 nm. The $CsPbBr_3$/CDs heterostructure spectrum covers a wider range, with peaks corresponding to both components, confirming retained luminescent properties. These comprehensive characterization results demonstrate the successful fabrication of the $CsPbBr_3$/CDs heterostructure, providing the material foundation for investigating its photonic synaptic properties.

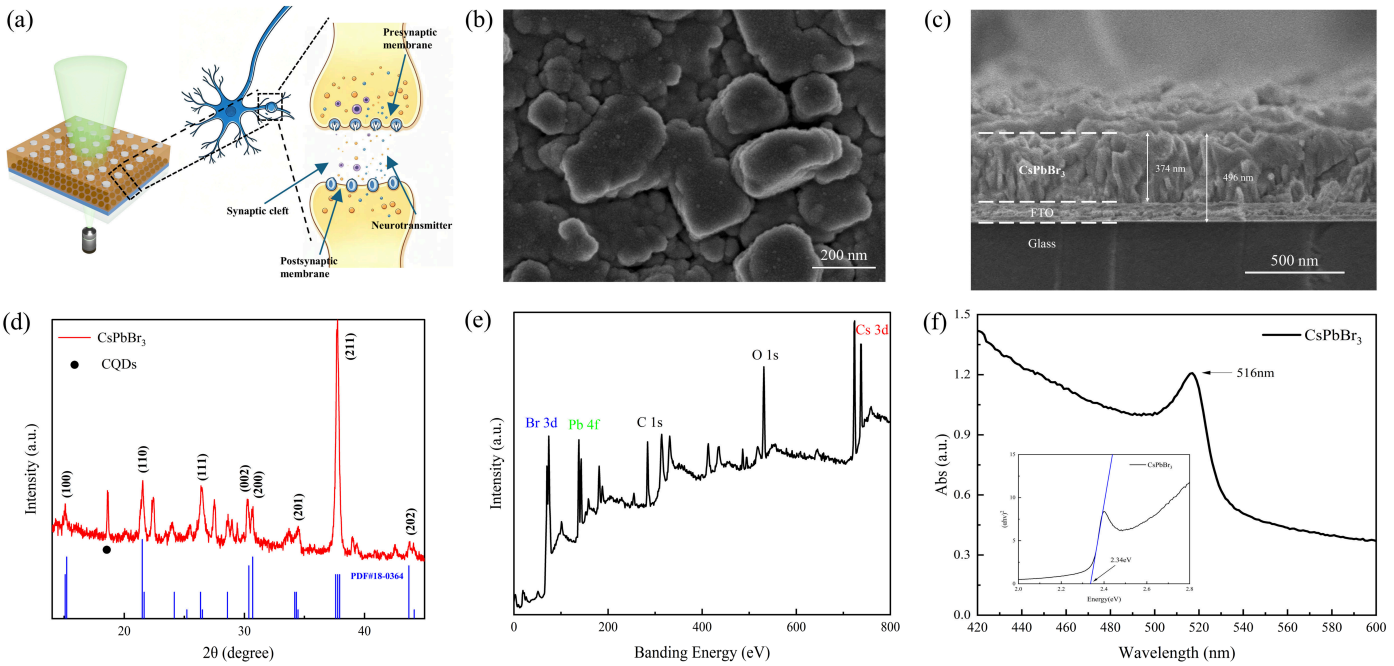


Figure 1. (**a**) Device schematic for synaptic emulation. (**b**) SEM image of surface $CsPbBr_3$ film. (**c**) Cross-sectional SEM images of $CsPbBr_3$-based structure. (**d**) XRD spectrum. (**e**) XPS spectra of $CsPbBr_3$ film. (**f**) Absorption spectra of $CsPbBr_3$ film (Tauc plot in inset).

We characterized the memristive behavior of $CsPbBr_3$-based devices using DC voltage sweeps. The Ag and FTO electrodes served as the anode and cathode, respectively. Voltage was cycled between 0 V → 1.5 V → 0 V → −1.5 V → 0 V with 100 mA current compliance. Figure 2a presents the dark current–voltage (I–V) curves for three distinct $CsPbBr_3$ memristor structures. All exhibit typical bipolar switching: transitioning from high-resistance state (HRS) to low-resistance state (LRS) during the positive sweep and reverting during the negative sweep. The $CsPbBr_3$/CDs structure demonstrates superior performance, with set

voltage (V_{set}) of 0.72 V (single structure: 0.81 V; CDs/$CsPbBr_3$: 1.17 V) and reset voltage (V_{reset}) of −0.6 V (single structure: −1.11 V; CDs/$CsPbBr_3$: −0.81 V). This configuration achieves a higher on/off ratio of 22 (single: 3; CDs/$CsPbBr_3$: 9) and enhanced stability over 50 cycles (Figure S4), indicating effective device improvement. Figure 2b shows the time dependent HRS and LRS currents for $CsPbBr_3$/CDs at −0.2 V. Both states remained stable for 10^4 s with the on/off ratio consistently maintained. The $CsPbBr_3$/CDs memristor maintains environmental stability following 90 days ambient storage, showing minimal state fluctuations (Figure S5), while characterization across 50 independently fabricated devices reveals consistent memristive switching with narrow voltage dispersion (V_{set}: 0.60 to 0.81 V; V_{reset}: −0.54 to −0.95 V), confirming high uniformity (Figure S6). The photoresponse was evaluated under 520 nm illumination (4 mW/cm^2). As shown in Figure 2c, all structures retained bipolar switching under light, with V_{set} values of 0.69 V ($CsPbBr_3$/CDs), 0.9 V (single structure), and 0.96 V (CDs/$CsPbBr_3$), and corresponding V_{reset} values of −0.48 V, −1.17 V, and −0.75 V. Compared to dark conditions (Figure S7), illumination reduced the operating voltages for devices, with $CsPbBr_3$/CDs exhibiting significantly lower values than the others. Stable bipolar switching over 50 cycles under illumination was observed for all structures (Figure S8). Figure 2d summarizes the V_{set} and V_{reset} distributions via box plots constructed from 50 consecutive switching cycles of individual devices for each structure, where boxes span the 25th–75th percentiles, central lines mark the median, and whiskers extend to 1.5 times the interquartile range. These results confirm the $CsPbBr_3$/CDs structure possesses the smallest operating voltages and demonstrate that the insertion position of CDs critically influences device performance.

To elucidate the carrier transport mechanism underlying the bipolar memristive behavior in fabricated devices, we analyzed log I–log V curves for Ag/$CsPbBr_3$/CDs/FTO under dark conditions via linear fitting (Figure 3a,b). During forward voltage scanning (Figure 3a), the device is initially in the HRS. In the low-voltage range, the fitting slope of the curve is approximately 1.07, a value that suggests that the conduction behavior of the device follows Ohm's law ($I \propto V$) [28]; this phenomenon is primarily attributed to the injection of thermally excited carriers. As the positive bias voltage is increased, the slope of the fitted curve shifts to approximately 2.65 and 2.10, indicating that the conduction mechanism is no longer Ohmic but is instead dominated by the space charge-limited current (SCLC) effect (Child's law: $I \propto V^2$) [29]. Within this voltage range, the traps inside the device are gradually filled to saturation by the injected carriers—a process that results in an exponential increase in carrier injection and a sharp rise in current, which in turn drives the device to transition from the HRS to the LRS. When the device is in the LRS, the fitting slope of the log I-log V curve is approximately 1.11, confirming that the conduction mechanism reverts to Ohm's law. In contrast, during the reset process (Figure 3b), when the device transitions from the LRS back to the HRS, its conduction mechanism is found to involve both Ohm's law and the SCLC mechanism. Similar analysis of the single-layer device (Figure 3c,d) revealed identical conduction mechanisms, with HRS reflecting intrinsic material conductivity and LRS Ohmic behavior suggesting metallic Ag filament formation in the switching layer. Subsequent fabrication with inert Pt electrodes yielded bipolar switching without distinct operating voltages (Figure S9), where Schottky emission dominated (Figure S10). Under 520 nm illumination, all three structures exhibited Ohmic and SCLC conduction mechanisms (Figure S11).

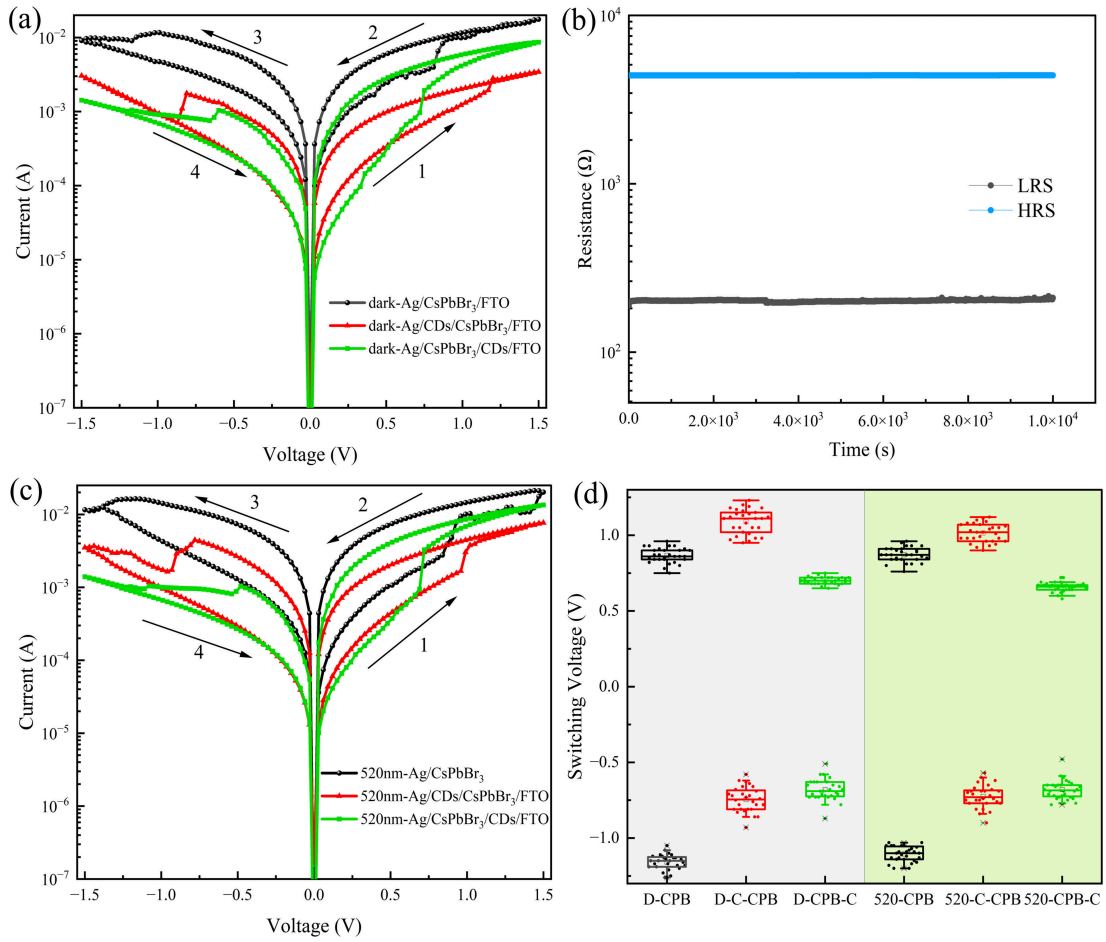


Figure 2. (**a**) I–V characteristics of the $CsPbBr_3$-based memristor under dark conditions. (**b**) The stability of the high- and low-resistance states for the Ag/$CsPbBr_3$/CDs/FTO device in dark. (**c**) I–V characteristics of the $CsPbBr_3$-based memristor under 520 nm illumination. (**d**) Switching voltage distributions across three device architectures.

Drawing on our previous theoretical findings, the plausible mechanism underlying the resistive switching process of $CsPbBr_3$ based devices is illustrated in Figure 4. Initially, ions are freely distributed within the memristive layer of the Ag/$CsPbBr_3$/FTO device (Figure 4a). Applying positive bias oxidizes the Ag electrode, generating Ag^+ ions that migrate towards the FTO electrode and reduce to Ag atoms. Continuous Ag accumulation ultimately forms conductive filaments bridging the electrodes. Driven by the external electric field, Br^- ions (possessing low activation energy) vacate their lattice sites, creating bromine vacancies (V_{Br}) [30]; these vacancies migrate towards the bottom electrode, establishing a conductive channel that transitions the device from HRS to LRS (Figure 4b). In the Ag/$CsPbBr_3$/CDs/FTO structure, the localized electric field enhancement effect of CDs generates a higher electric field intensity around these nanostructures than in other regions of the device. This enhanced electric field significantly accelerates the migration rates of Ag^+ and V_{Br} in the vicinity of the CDs, inducing preferential filament formation (Figure 4c) and reducing V_{set}. Conversely, in the Ag/CDs/$CsPbBr_3$/FTO structure, the CDs layer resides between the Ag electrode and $CsPbBr_3$. Surface defects on the CDs capture injected electrons, impeding Ag oxidation, while the generated Ag^+ must traverse the CDs layer to reach the functional layer. These combined effects delay conductive channel formation, resulting in the highest V_{set} for this configuration. Applying negative bias, the Ag atoms and V_{Br} within the filaments to migrate back towards Ag electrode, rupturing the filaments and resetting the device from LRS to HRS. The local field enhancement by

CDs in the Ag/$CsPbBr_3$/CDs/FTO device similarly accelerates Ag atom and V_{Br} migration under reverse bias, enabling more efficient filament rupture (Figure 4d) and consequently a lower V_{reset}. Under illumination, photo-generated electron–hole pairs in the $CsPbBr_3$ film separate within the applied field, increasing ion concentration in the functional layer and thereby accelerating both filament formation and rupture processes (Figure 4e), leading to lower operating voltages.

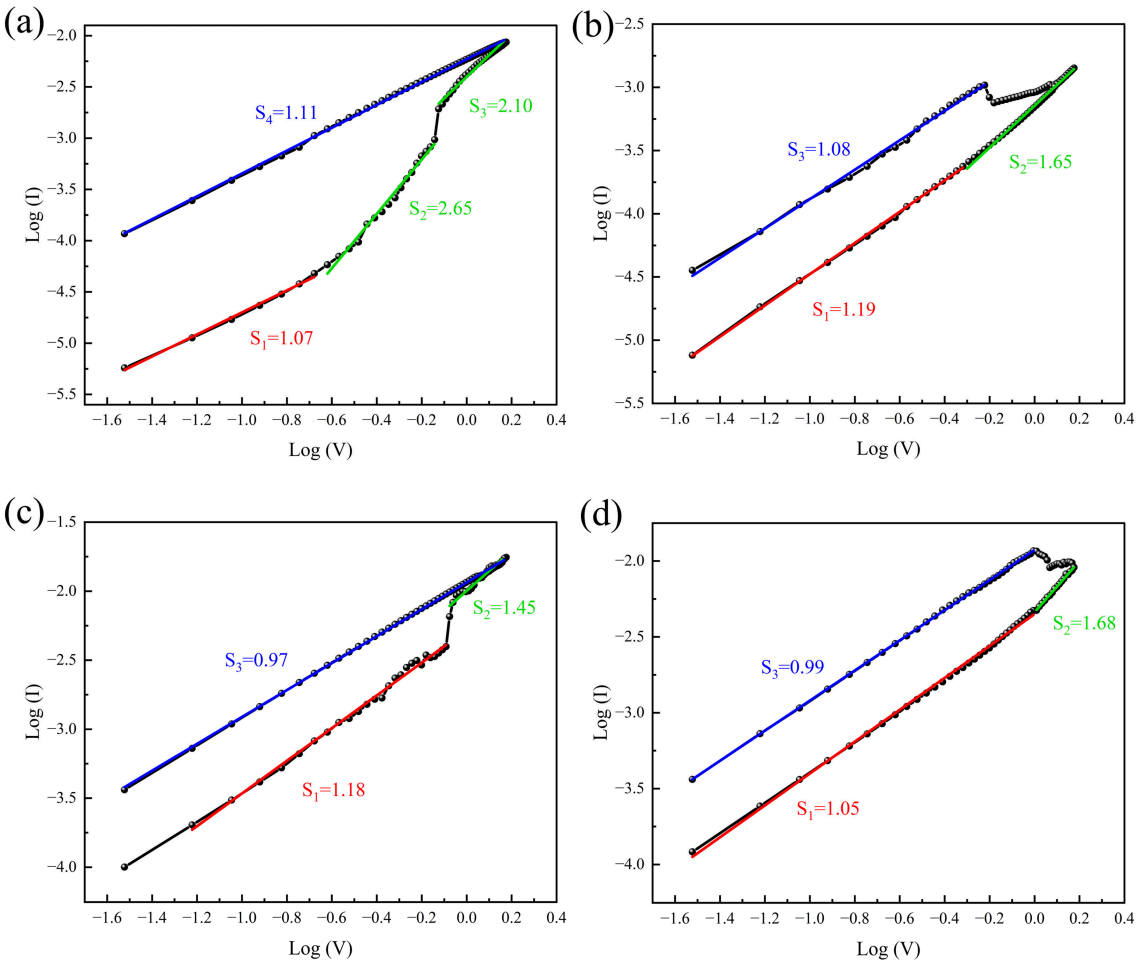


Figure 3. Logarithmic current–voltage characteristics for (**a**) SET and (**b**) RESET switching sweeps: (**a**,**b**) Ag/$CsPbBr_3$/CDs/FTO device; (**c**,**d**) Ag/$CsPbBr_3$/FTO device.

We further investigated optoelectronic synaptic emulation in Ag/$CsPbBr_3$/CDs/FTO devices designed to mimic biological counterparts. Synaptic plasticity was replicated through progressive conductance tuning via 10 ms voltage spike trains applied to the Ag top electrode, simulating neurotransmitter-mediated signal relaying between neurons. Figure 5a illustrates conductance changes under ±0.1 V voltage pulses (10 ms interval/width) applied to the Ag electrode (simulating presynaptic input). Conductance increased progressively under positive pulses, emulating LTP and decreased under negative pulses, corresponding to LTD. Repeatable conductance modulation over multiple cycles confirmed stable LTP/LTD simulation. Figure 5b presents paired-pulse facilitation (PPF) results, where the PPF index decayed with increasing inter-pulse interval (Δt = 10–50 ms). Fitting yielded a characteristic time constant τ = 22.53 ms, indicating short-term

plasticity emulation. The diminished facilitation at longer Δt reflects recombination/release of transient carriers between pulses. PPF% was calculated as follows [31]:

$$\text{PPF\%} = \frac{A_1 - A_2}{A_1} \times 100\% \quad (1)$$

where A_1 and A_2 represent the amplitudes of the first and second pulse responses, respectively.

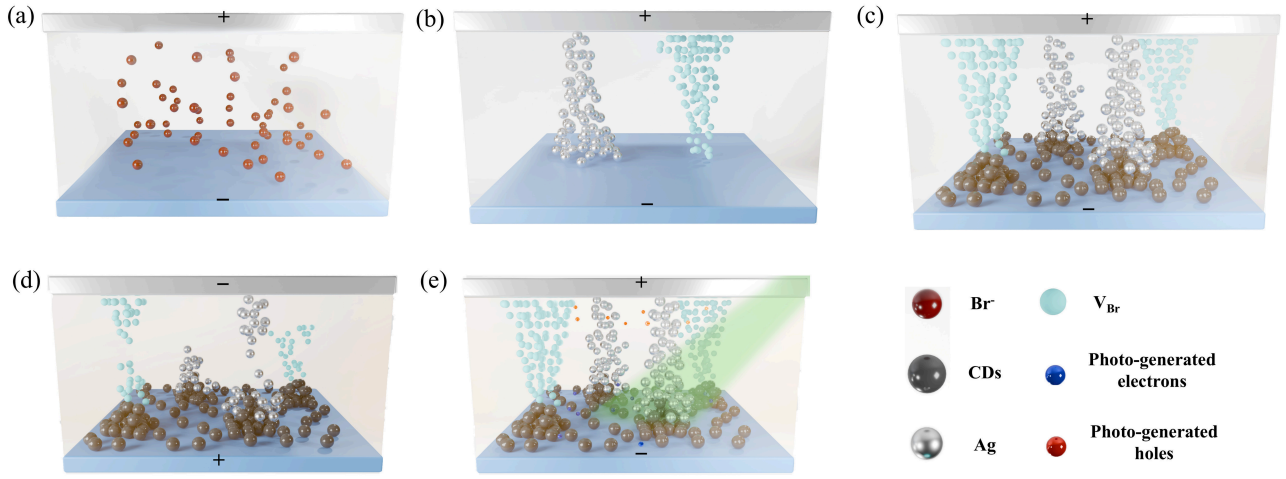


Figure 4. A schematic diagram of the memristive behavior: (**a**) pristine state and (**b**) LRS of Ag/$CsPbBr_3$/FTO device. (**c**) LRS and (**d**) HRS of Ag/$CsPbBr_3$/CDs/FTO device. (**e**) LRS of Ag/$CsPbBr_3$/CDs/FTO device under 520 nm illumination.

Spike timing-dependent plasticity (STDP) is a crucial Hebbian learning rule in neural systems, where synaptic weight modification depends on the timing difference between pre- and post-synaptic spikes [32]. The synaptic weight change rate (ΔW) is calculated as follows [33]:

$$\Delta W = \frac{W_{STDP} - W_0}{W_0} \times 100\% \quad (2)$$

where W_0 and W_{STDP} are the conductance values before and after pulse application, respectively. Figure 5c presents the STDP characteristics of the device, which were measured by applying presynaptic pulses (0.5 V) to the top electrode and postsynaptic pulses (−0.5 V) to the bottom electrode, with a read voltage of 0.1 V used to monitor conductance changes during testing. LTP occurs when presynaptic spikes precede postsynaptic spikes ($\Delta t > 0$), whereas LTD emerges when postsynaptic spikes arrive before presynaptic spikes ($\Delta t < 0$). the device exhibits synaptic weight depression. This behavior follows the asymmetric Hebbian STDP rule:

$$\Delta W = \begin{cases} A_+ \, exp(-\Delta t/\tau_+), \Delta t > 0 \\ -A_- \, exp(\Delta t/\tau_-), \Delta t < 0 \end{cases} \quad (3)$$

where A_+ and A_- are scaling factors, and τ_+ and τ_- are time constants. Fitting results yielded A_+ = 120.41% and τ_+ = 32.32 ms for $\Delta t > 0$, and A_- = 113.64% and τ_- = 28.77 ms for $\Delta t < 0$.

These millisecond-range time constants are comparable to the temporal response characteristics of biological synapses, indicating the device's suitability for simulating timing-dependent learning behaviors.

Figure 5d,e show the electrical potentiation and depression curves of the device under continuous electrical pulse stimulation, respectively. Current gradually increased and saturated under positive pulses (0.1 V), indicating the progressive formation of conductive channel transport paths, while current gradually decreased under negative pulses

(0.1 V), indicating the weakening of conductive channels. The continuous, non-abrupt change in current with pulse number facilitates multi-level weight modulation in neural network hardware.

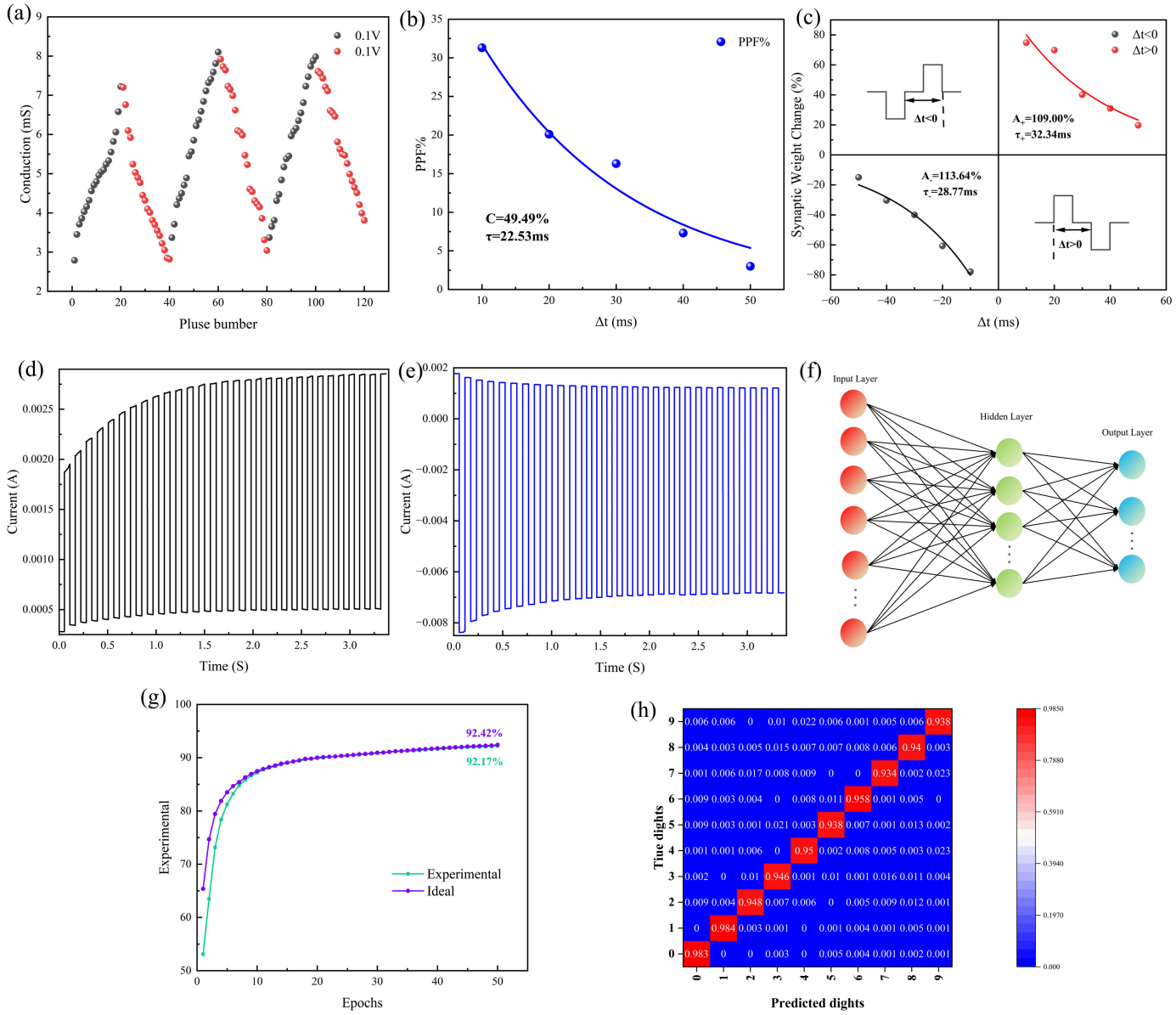


Figure 5. (**a**) Conductance modulation of Ag/$CsPbBr_3$/CDs/FTO device under voltage pulses. (**b**) PPF characteristics. (**c**) STDP response. (**d**) Electrical potentiation, and (**e**) depression under continuous electrical pulse stimulation. (**f**) ANN schematic for 28 × 28-pixel handwritten digit recognition. (**g**) Photopic adaptation-dependent recognition rate evolution versus time. (**h**) Result of confusion matrix for 0–9 digits.

Leveraging the LTP/LTD characteristics, we constructed a three-layer artificial neural network (ANN), as illustrated in Figure 5f, which consists of an input layer with 784 neurons, a hidden layer with 256 neurons, and an output layer with 10 neurons. This ANN was then used to train and recognize 28 × 28-pixel handwritten digit images, which were obtained from the modified National Institute of Standards and Technology (MNIST) dataset. During the training process, the 784-neuron input layer directly corresponds to the 28 × 28 pixels of individual MNIST images. The 256 hidden neurons perform nonlinear transformations to extract and integrate features from the input data, while the 10 output neurons have a one-to-one correspondence with the digits 0–9. Figure 5g shows recognition

accuracy rising and stabilizing with training epochs. The device achieved 92.17% accuracy—approaching the 92.42% benchmark of ideal synaptic devices—validating its capability for high-precision weight updates. Figure 5h presents the confusion matrix, revealing high accuracy across digits 0–9 (peak: 98.3% for "1"; minimum: 93.4% for "7"). These results underscore the Ag/$CsPbBr_3$/CDs/FTO device's potential for neuromorphic computing and visual recognition systems.

4. Conclusions

In this work, we successfully fabricated an optoelectronic memristor based on a carbon dot-modified Ag/$CsPbBr_3$/CDs/FTO heterostructure. Compared to other device architectures, this structure demonstrates significantly enhanced memristive performance, characterized by substantially reduced operating voltages (set/reset voltages of 0.72 V/−0.60 V) and preliminary cycling endurance with stable state retention; however, the current cycling endurance remains limited to 50 cycles. Mechanistic studies revealed that the carbon dot layer functions as an effective charge-trapping center through its abundant surface defect states. Furthermore, by promoting localized electric field convergence, it guides the formation and rupture of silver conductive filaments at lower voltages, enabling highly stable, low-voltage switching operations. Leveraging continuous multilevel conductance state modulation, the device successfully emulated fundamental synaptic plasticity behaviors, including long-term potentiation and depression. When implemented in an artificial neural network for handwritten digit classification, it achieved a recognition accuracy of 92.17%. This work effectively regulates the performance of perovskite memristors through carbon dot interface engineering, establishing a novel material and structural strategy for developing low-power, high-performance neuromorphic optoelectronic synaptic devices, though the cycling endurance limitation currently constrains its applicability in neuromorphic hardware.

Supplementary Materials: The following supporting information can be downloaded at: https://www.mdpi.com/article/10.3390/coatings16101221/s1, Figures S1–S3 present characterization spectra of $CsPbBr_3$ films and CDs, including HRXPS, UV-vis absorption, and PL spectra; Figures S4–S9 and S11 display I–V characteristics, endurance tests, and stability evaluations of perovskite-based devices with varying architectures under dark and illuminated conditions; Figure S10 illustrates conduction mechanisms governed by Schottky emission.

Author Contributions: Conceptualization, H.Z. and G.W.; Methodology, Q.X. and G.W.; Software, L.Z.; Validation, Y.F., C.S. and G.W.; Investigation, Y.F., C.S., K.W., Q.X. and G.W.; Resources, G.W.; Data curation, Y.F., C.S., L.Z. and K.W.; Writing—original draft, Y.F. and G.W.; Writing—review & editing, H.Z., Q.X. and G.W.; Visualization, L.Z.; Supervision, Q.X. and G.W.; Project administration, G.W.; Funding acquisition, H.Z., Q.X. and G.W. All authors have read and agreed to the published version of the manuscript.

Funding: This work was supported by the National Natural Science Foundation of China (12374112), the Natural Science Foundation of Shandong Province (ZR2023QA095), the Fundamental Research Program of Shanxi Province, China (Grant No. 202303021222115).

Data Availability Statement: The original contributions presented in this study are included in the article and Supplementary Material. Further inquiries can be directed to the corresponding authors.

Conflicts of Interest: The authors declare no conflict of interest.

References

1. Zidan, M.A.; Strachan, J.P.; Lu, W.D. The future of electronics based on memristive systems. *Nat. Electron.* **2018**, *1*, 22–29. [CrossRef]
2. Ielmini, D.; Wong, H.S.P. In-memory computing with resistive switching devices. *Nat. Electron.* **2018**, *1*, 333–343. [CrossRef]

3. Yao, Y.C.; Lee, C.J.; Chen, Y.J.; Feng, J.Z.; Oh, H.; Lue, C.S.; Sheu, J.K.; Lee, Y.J. All-Inorganic Perovskite Quantum-Dot Optical Neuromorphic Synapses for Near-Sensor Colored Image Recognition. *Adv. Sci.* **2025**, *12*, e2409933. [CrossRef]
4. Strukov, D.B.; Snider, G.S.; Stewart, D.R.; Williams, R.S. The missing memristor found. *Nature* **2008**, *453*, 80–83. Erratum in *Nature* **2009**, *459*, 1154. [CrossRef]
5. Jo, S.H.; Chang, T.; Ebong, I.; Bhadviya, B.B.; Mazumder, P.; Lu, W. Nanoscale memristor device as synapse in neuromorphic systems. *Nano Lett.* **2010**, *10*, 1297–1301. [CrossRef]
6. Zhang, G.; Zeng, Z.; Yan, Y.; Tang, J.; Wang, H.; Su, C.; Yi, X.; Zhang, X.; Hu, Y.; Chen, H. Ultraviolet-Regulated Synaptic-Neuronal Function Reconfigurable Transparent Memristor for Neuromorphic Computing Hardware. *Adv. Funct. Mater.* **2026**, *36*, e31113. [CrossRef]
7. Cui, D.; Pei, M.; Lin, Z.; Zhang, H.; Kang, M.; Wang, Y.; Gao, X.; Su, J.; Miao, J.; Li, Y.; et al. Versatile optoelectronic memristor based on wide-bandgap Ga_2O_3 for artificial synapses and neuromorphic computing. *Light Sci. Appl.* **2025**, *14*, 161. [CrossRef]
8. Niu, J.; Liu, Z.; Ding, X.; Meng, Z.; Li, X.; Deng, J.; Wang, W.; Lu, F. All-Optical Artificial Synapse Based on ε-Ga_2O_3 and β-Ga_2O_3 Mixed-Phase Thin Films. *Materials* **2026**, *19*, 711. [CrossRef]
9. Yan, H.; Zhuang, P.; Li, B.; Ye, T.; Zhou, C.; Chen, Y.; Li, T.; Cai, W.; Yu, D.; Liu, J.; et al. Metal Penetration and Grain Boundary in MoS_2 Memristors. *Adv. Electron. Mater.* **2024**, *11*, 2400264. [CrossRef]
10. Fu, S.; Park, J.H.; Gao, H.; Zhang, T.; Ji, X.; Fu, T.; Sun, L.; Kong, J.; Yao, J. Two-Terminal MoS_2 Memristor and the Homogeneous Integration with a MoS_2 Transistor for Neural Networks. *Nano Lett.* **2023**, *23*, 5869–5876. [CrossRef]
11. Zhang, L.; Zeng, C.; Gong, X.; Shu, L.; Zhu, Y.; Xu, Y.; Lin, W.; Zhuang, P. A scalable thermal route to WS_2 for high-endurance memristors with engineered volatility. *Appl. Mater. Today* **2026**, *52*, 103386. [CrossRef]
12. Tanisha, T.T.; Hassan, O.; Alam, M.K. Doping-induced performance optimization in monolayer WS_2 memristor: Reduced variability and contact resistance. *RSC Adv.* **2025**, *15*, 26052–26064. [CrossRef]
13. Chaudhary, T.; Kaur, D. Revealing the potential of 2D WS_2 memristors as an artificial synapse with resilient gradual behavior at high temperatures for neuromorphic applications. *Nanoscale Horiz.* **2026**, *11*, 1662–1675. [CrossRef]
14. Liang, H.-N.; Bai, N.; Zou, L.-Q.; Sun, H.-J.; Xue, K.-H.; Cheng, W.-M.; Lu, H.; Miao, X.-S. Resistive Switching Characteristics of HfO_x-Based Memristor by Inserting GeTe Layer. *IEEE Trans. Electron. Devices* **2023**, *70*, 83–87. [CrossRef]
15. Yang, Y.; Yang, Y.; Xiong, S.; Wang, Y.; Hu, K.; Wang, F.; Li, X.; Feng, L.; Guo, H.; Zheng, L.; et al. Bio-Inspired Sb_2S_3 Memristors Supporting Dual-Mode Operation via Self-Regulating Transport Pathways for All-in-one Neuromorphic Perception and Computation. *Adv. Funct. Mater.* **2025**, *36*, e10212. [CrossRef]
16. Kundale, S.S.; Pawar, P.S.; Kumbhar, D.D.; Devara, I.K.G.; Sharma, I.; Patil, P.R.; Lestari, W.A.; Shim, S.; Park, J.; Dongale, T.D.; et al. Multilevel Conductance States of Vapor-Transport-Deposited Sb_2S_3 Memristors Achieved via Electrical and Optical Modulation. *Adv. Sci.* **2024**, *11*, e2405251. [CrossRef]
17. Bowman, A.R.; Yuan, Q.; Lilly, J.R.S.; Wood, A.T.M.; Lim, V.J.-Y.; Johnston, M.B.; Noel, N.K.; Herz, L.M. Degradation dynamics of lead-halide perovskites under combined heat and light. *Energy Environ. Sci.* **2026**. [CrossRef]
18. Lu, Z.; Lou, C.; Cheng, A.; Zhang, J.; Sun, J. A sensitive and ultrafast $FA_{0.83}Cs_{0.17}PbI_3$ perovskite sensor for NO_2 detection at room temperature. *J. Alloys Compd.* **2022**, *919*, 165831. [CrossRef]
19. Uhm, J.; Byun, Y.; Park, S.; Kim, S.; Choi, M.J. Iodide-Coated $CsPbBr_3$ Perovskite Nanowires for Resistive-Switching Memory in Neuromorphic Systems and Edge Computing. *Nano Lett.* **2026**, *26*, 3503–3513. [CrossRef]
20. Xie, Z.; Wu, J.; Tian, J.; Li, C.; Zhang, D.; Chen, L.; Loi, M.A.; Osvet, A.; Brabec, C.J. Additive-Engineered CsPbBr(3)-Based Perovskite Memristors for Neuromorphic Computing and Associative Learning Applications. *ACS Appl. Mater. Interfaces* **2025**, *17*, 53704–53715. [CrossRef]
21. Mondal, S. Carbon dots as photosensitizers: Unraveling their ultrafast charge transfer, challenges, and future prospects. *Nanoscale Adv.* **2026**, *8*, 782–793. [CrossRef]
22. Zhao, M.; Shi, Y.; Dai, J.; Lian, J. Ellipsometric study of the complex optical constants of a $CsPbBr_3$ perovskite thin film. *J. Mater. Chem. C* **2018**, *6*, 10450–10455. [CrossRef]
23. Paul, T.; Chatterjee, B.K.; Maiti, S.; Sarkar, S.; Besra, N.; Das, B.K.; Panigrahi, K.J.; Thakur, S.; Ghoraid, U.K.; Chattopadhyay, K.K. Tunable cathodoluminescence over the entire visible window from all-inorganic perovskite $CsPbX_3$ 1D architecture. *J. Mater. Chem. C* **2018**, *6*, 3322. [CrossRef]
24. Shen, S.; Fu, J.; Wang, H. A Facile, Effective Synthesis of Excellent Fluorescent Carbon Dots with Optical Properties. *ChemistrySelect* **2019**, *4*, 12762–12767. [CrossRef]
25. Chen, R.; Liang, Z.; Feng, W.; Hu, X.; Hao, A. Solution-processed all-inorganic perovskite $CsPbBr_3$ thin films for optoelectronic application. *J. Alloys Compd.* **2021**, *864*, 158125. [CrossRef]
26. Lin, Q.; Hu, W.; Zang, Z.; Zhou, M.; Du, J.; Wang, M.; Han, S.; Tang, X. Transient Resistive Switching Memory of $CsPbBr_3$ Thin Films. *Adv. Electron. Mater.* **2018**, *4*, 1700596. [CrossRef]
27. Delsouz Chahardeh, M.; Shakeri, A. Nitrogen-Doped Carbon Quantum Dot as Novel Nano Additive to Improve Performance and Fouling Resistance of Forward Osmosis Thin Film Nanocomposite Membranes. *Polym. Adv. Technol.* **2025**, *36*, e70158. [CrossRef]

28. Luo, F.; Zhong, W.-M.; Tang, X.-G.; Chen, J.-Y.; Jiang, Y.-P.; Liu, Q.-X. Application of artificial synapse based on all-inorganic perovskite memristor in neuromorphic computing. *Nano Mater. Sci.* **2024**, *6*, 68–76. [CrossRef]
29. Zhu, Y.; Chen, M.; Lu, H.; Mi, P.; Luo, D.; Wang, Y.; Liu, Y.; Xiong, R.; Wang, H. The filaments control for tunning digital resistive switching in data storage application and analog behavior as an artificial synapse with $CsPbBr_3$-based memristor. *Appl. Phys. Lett.* **2024**, *124*, 063504. [CrossRef]
30. Zhang, G.; Xu, Y.; Yang, S.; Ren, S.; Jiao, Y.; Wang, Y.; Ma, X.; Li, H.; Hao, W.; He, C.; et al. Robust mica perovskite photoelectric resistive switching memory. *Nano Energy* **2023**, *106*, 108074. [CrossRef]
31. Kim, M.K.; Lee, J.S. Short-Term Plasticity and Long-Term Potentiation in Artificial Biosynapses with Diffusive Dynamics. *ACS Nano* **2018**, *12*, 1680–1687. [CrossRef]
32. Shooshtari, M.; Kim, S.-Y.; Pahlavan, S.; Serrano-Gotarredona, T.; Bisquert, J.; Linares-Barranco, B. Bio-Inspired Spike-Timing-Dependent Plasticity Learning with Metal Halide Perovskites: Toward Artificial Synaptic Functionality. *ACS Appl. Mater. Interfaces* **2026**, *18*, 7103–7114. [CrossRef]
33. Liu, L.; Cheng, Z.; Jiang, B.; Liu, Y.; Zhang, Y.; Yang, F.; Wang, J.; Yu, X.F.; Chu, P.K.; Ye, C. Optoelectronic Artificial Synapses Based on Two-Dimensional Transitional-Metal Trichalcogenide. *ACS Appl. Mater. Interfaces* **2021**, *13*, 30797–30805. [CrossRef]

Disclaimer/Publisher's Note: The statements, opinions and data contained in all publications are solely those of the individual author(s) and contributor(s) and not of MDPI and/or the editor(s). MDPI and/or the editor(s) disclaim responsibility for any injury to people or property resulting from any ideas, methods, instructions or products referred to in the content.